Study of Plasma Heating Processes in a Coronal Mass Ejection–driven Shock Sheath Region Observed with the Metis Coronagraph

Federica Frassati[1] , Alessandro Bemporad[1] , Salvatore Mancuso[1] , Silvio Giordano[1] , Vincenzo Andretta[2] , Aleksandr Burtovoi[3,4] , Vania Da Deppo[5] , Yara De Leo[6] , Silvano Fineschi[1] , Catia Grimani[7] , Salvo Guglielmino[8] , Petr Heinzel[9,10] , Giovanna Jerse[11] , Federico Landini[1] , Alessandro Liberatore[12] , Giampiero Naletto[13] , Gianalfredo Nicolini[1] , Maurizio Pancrazzi[1] , Paolo Romano[8] , Marco Romoli[4] , Giuliana Russano[2] , Clementina Sasso[2] , Daniele Spadaro[8] , Marco Stangalini[14] , Roberto Susino[1] , Luca Teriaca[6] , Michela Uslenghi[15] , and Luca Zangrilli[1]

[1] INAF—Osservatorio Astrofisico di Torino, Via Osservatorio 20, 10025 Pino Torinese (TO), Italy; federica.frassati@inaf.it
[2] INAF—Osservatorio Astronomico di Capodimonte, Salita Moiarello 16, 80131 Napoli, Italy
[3] INAF—Osservatorio Astrofisico di Arcetri, Largo Fermi 5, 50125 Firenze, Italy
[4] Dip. di Fisica e Astronomia, Università di Firenze, Via Sansone 1, 50019 Sesto Fiorentino (FI), Italy
[5] CNR—IFN, Via Trasea 7, 35131 Padova, Italy
[6] Max Planck Institute for Solar System Research, Justus-von-Liebig-Weg 3, 37077 Göttingen, Germany
[7] Dip. di Scienze Pure e Applicate, Università di Urbino, Via Santa Chiara, 27, 61029 Urbino, Italy
[8] INAF—Osservatorio Astrofisico di Catania, Via Santa Sofia 78, 95123 Catania, Italy
[9] Academy of Science of the Czech Republic, Fričova 298, 251 65 Ondřejov, Czech Republic
[10] University of Wroclaw, Center of Scientific Excellence—Solar and Stellar Activity, Kopernika 11, 51-622 Wroclaw, Poland
[11] INAF—Osservatorio Astronomico di Trieste, Via G.B. Tiepolo 11, 34143 Trieste, Italy
[12] Jet Propulsion Laboratory, California Institute of Technology, Pasadena, CA 91109, USA
[13] Dip. di Fisica e Astronomia, Università di Padova, Via F. Marzolo, 8-35131 Padova, Italy
[14] ASI, Via del Politecnico, 00133 Roma, Italy
[15] INAF—IASF Milano, Via Alfonso Corti 12, 20133 Milano, Italy

Abstract

On 2021 September 28, a C1.6 class flare occurred in active region NOAA 12871, located approximately at 27°S and 51°W on the solar disk with respect to Earth's point of view. This event was followed by a partial halo coronal mass ejection (CME) that caused the deflection of preexisting coronal streamer structures, as observed in visible-light coronagraphic images. An associated type II radio burst was also detected by both space- and ground-based instruments, indicating the presence of a coronal shock propagating into interplanetary space. By using H I Lyα (121.6 nm) observations from the Metis coronagraph on board the Solar Orbiter mission, we demonstrate for the first time the capability of UV imaging to provide, via a Doppler dimming technique, an upper limit estimate of the evolution of the 2D proton kinetic temperature in the CME-driven shock sheath as it passes through the field of view of the instrument. Our results suggest that over the 22 minutes of observations, the shock propagated with a speed decreasing from about 740 ± 110 km s^{-1} to 400 ± 60 km s^{-1}. At the same time, the postshock proton temperatures peaked at latitudes around the shock nose and decreased with time from about 6.8 ± 1.01 MK to 3.1 ± 0.47 MK. The application of the Rankine–Hugoniot jump conditions demonstrates that these temperatures are higher by a factor of about 2–5 than those expected from simple adiabatic compression, implying that significant shock heating is still going on at these distances.

1. Introduction

Every day the Sun exhibits spectacular transient phenomena such as flares, prominence eruptions, and coronal mass ejections (CMEs), as well as concurrent phenomena such as shock waves and solar energetic particle events. Continuous monitoring of our star serves a dual purpose: first, it enhances our comprehension of the source and evolution of the abovementioned phenomena to advance our understanding of enigmatic plasma physical processes; second, it deepens our familiarity with these events in terms of their effects on our technology and biological systems.

The main tools that are useful to continuously monitor the Sun and its atmosphere are space-based instruments. In particular, CMEs, first identified in 1971 by Hansen et al. (1971), have been observed and analyzed since then by both ground- and space-based coronagraphs. These instruments gauge the emission of visible light (VL) produced by Thomson scattering of photospheric radiation by free electrons in the solar corona, also known as K-corona emission. By studying the polarized brightness of the VL emission, it becomes feasible to deduce the local plasma column and number densities, and to approximate the expansion velocity as well as the projected and unprojected acceleration of solar eruptions. On the other hand, certain critical plasma parameters, such as temperature distributions and elemental abundances, cannot be ascertained solely from VL observations: data collected at various wavelengths from the E-corona (or ion line emission), mostly in the extreme-ultraviolet (EUV), are also essential for a comprehensive analysis.

(a)   (b)
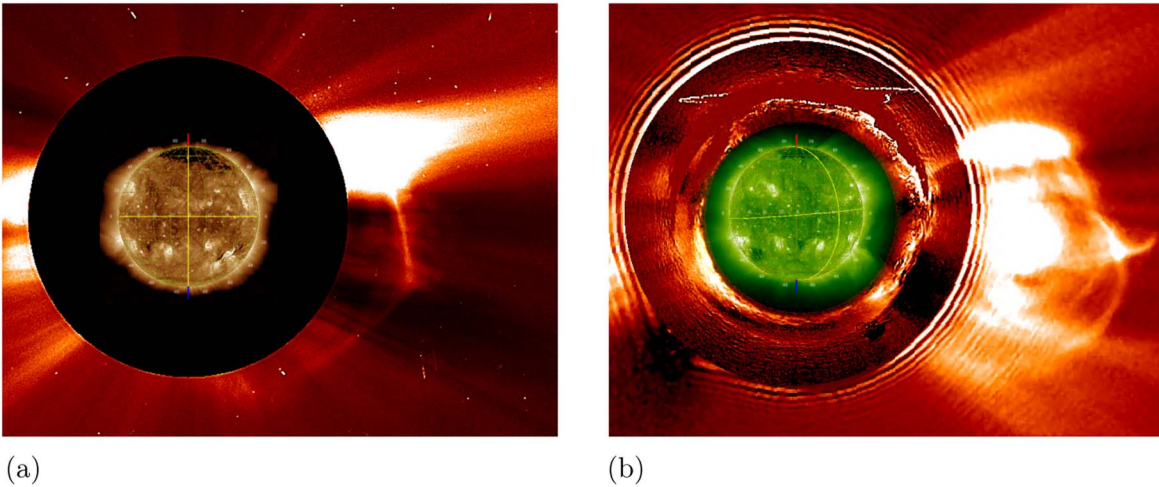
Figure 1. The expanding CME structure as seen by LASCO-C2 combined with AIA (193 Å) (a) and STEREO-A/SECCHI instruments (b). These images were created by using the JHelioviewer visualization tool (Müller et al. 2017).

By combining VL observations from the Large Angle and Spectrometric Coronagraph (LASCO; Brueckner et al. 1995) and UV data from the UV Coronagraph Spectrometer (UVCS; Kohl et al. 1995) mounted on the Solar and Heliospheric Observatory (Domingo et al. 1995), significant results were achieved about CMEs. These include insights into their internal plasma temperature distribution, the elemental composition within them, and their evolution (both core and front; e.g., Akmal et al. 2001; Ciaravella et al. 2003; Raymond et al. 2003; Bemporad et al. 2007), post-CME current sheets (e.g., Bemporad 2008; Cai et al. 2016), CME-driven shocks (e.g., Mancuso et al. 2002; Mancuso & Avetta 2008; Bemporad & Mancuso 2010; Mancuso 2011; Bemporad et al. 2014), and 3D and spectroscopic reconstructions (Susino et al. 2014). A comprehensive catalog of events studied with UVCS was compiled by Giordano et al. (2013). According to the findings of Manchester et al. (2012), the thermodynamics for protons and electrons are expected to be different. This is due to the fact that shocks are only supersonic relative to the speed of the proton fast mode and not to that of the electrons. In particular, protons absorb the kinetic energy dissipated at the shock, whereas electrons, when encountering the shock, undergo only heating through adiabatic compression. On the other hand, it is important to point out that the determination of the CME plasma temperature distribution and of the elemental abundances during the expansion phase in the intermediate corona, as determined by the UVCS spectrometer, were confined to the limited field of view (FOV) of its entrance slit.

On 2020 February 10, a significant advancement took place in the field of solar physics: the Metis instrument (Antonucci et al. 2020, Fineschi et al. 2020), on board the Solar Orbiter (Müller et al. 2020) spacecraft, was launched. This marked the initiation of a new phase, enabling the observation of the solar corona using a multichannel imaging coronagraph. This innovative instrument is capable of concurrently observing the solar corona in two distinct spectral bands: a UV narrow band centered around the Lyα line (121.6 nm) generated by neutral hydrogen atoms, and the polarized VL in the wavelength range 580–640 nm. The Metis instrument has a square FOV spanning $\pm 2.9°$ in width, limited by an inner circular FOV of $1.6°$ produced by the occultation system for the Sun's disk. During the eccentric orbits of Solar Orbiter, this configuration allows Metis to survey the solar corona in a range from 1.7 solar radii ($R_\odot$) at perihelion up

to approximately 9 $R_\odot$ at aphelion. The primary objective of Metis is to track the dynamic processes and evolutionary changes in the solar corona, achieving exceptional temporal and spatial resolution.

In order to showcase the potential of Metis to infer the CME/CME-driven shock density and temperature by combining VL and UV images instead of line intensities from spectrometers, many studies have been conducted with data acquired before the start of the mission (e.g., Susino & Bemporad 2016; Bemporad et al. 2018; Ying et al. 2020; Bemporad 2022). Notably, the technique of Doppler dimming (Hyder & Lites 1970; Withbroe et al. 1982) was employed to estimate the temperature. In this study, we introduce the novel utilization of UV coronagraphic images acquired by Metis. These images enable us for the first time to make an estimation of the upper limit of the evolution of the 2D proton kinetic temperature in the CME-driven shock sheath. The structure of the paper is outlined as follows: we detail the event by using observations at different wavelengths (Section 2), we conduct an analysis of the UV data (Section 3), and we finally discuss the results and draw our conclusions (Section 4).

2. Observations

A C1.6 class solar flare occurred on 2021 September 28, as observed by the Geostationary Operational Environmental Satellite in soft X-rays, initiating at 05:54 UT and reaching its peak around 06:34 UT. This flare was identified within the active region NOAA 12871 with respect to Earth's point of view, situated approximately at coordinates 27°S and 51°W, as observed by the Atmospheric Imaging Assembly (AIA; Lemen et al. 2012) instrument aboard the Solar Dynamics Observatory. The event included a partial halo CME, which deflected the preexisting coronal streamer structures, as inferred from LASCO coronagraphic images. No event-related prominence was observed.

The CME entered the FOV of the LASCO-C2 coronagraph at 06:48 UT and was observed as a partial halo of width ∼265° off the west limb (with central position angle at 206°) as shown in Figure 1(a). The same expanding front was also observed by the Extreme Ultraviolet Imager (EUVI), COR1, and COR2 coronagraphs on the Sun Earth Connection Coronal and Heliospheric Investigation (SECCHI) on board STEREO-A. At
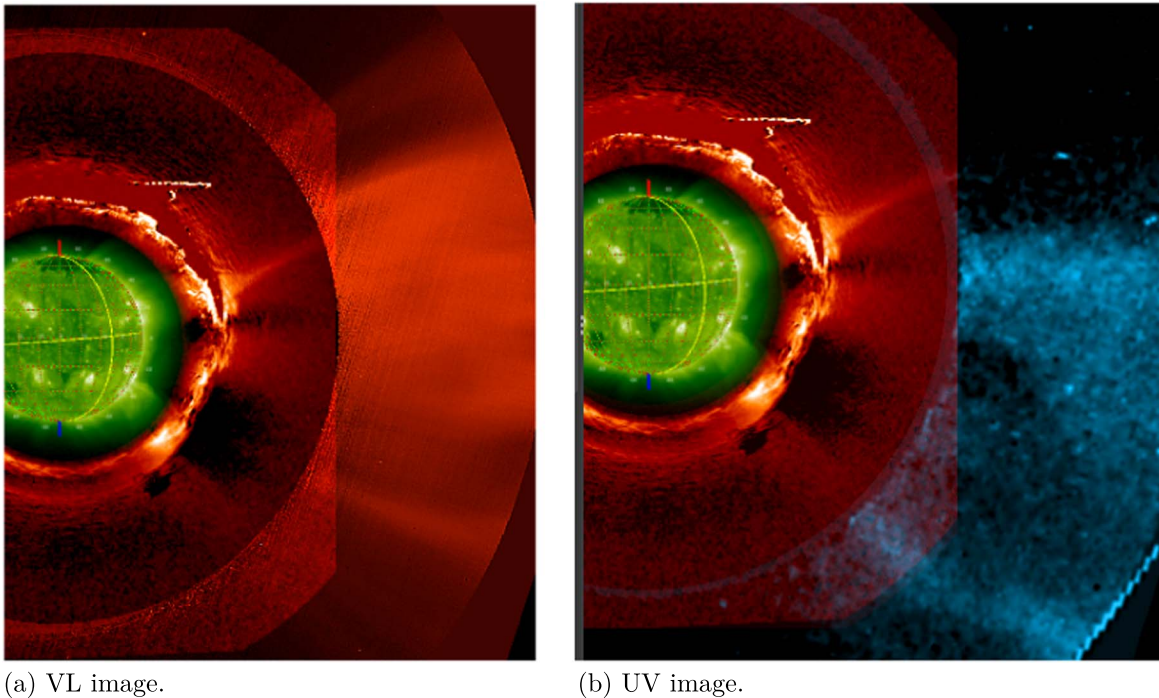
(a) VL image.   (b) UV image.

Figure 2. The CME as seen by the VL (a) and UV Lyα (b) channels of Solar Orbiter/Metis coronagraph at 07:35 and 07:33 UT, respectively. In the VL channel, the blurring effect is evident due to the parameters that were set for the observation. The normalizing-radial-graded filter (Morgan et al. 2006) was applied to both images in order to enhance the coronal structures. To visualize the Sun's disk, as no observations were planned for the Full Sun Imager/Extreme Ultraviolet Imager (FSI/EUI) on board the Solar Orbiter, the STEREO-A/SECCHI EUVI195 and COR1 were used. These images were created by using the JHelioviewer visualization tool (Müller et al. 2017).

that time, the spacecraft's longitudinal separation from Earth was approximately 39.44° east. From STEREO-A's point of view, the event occurred at the western limb, as shown in Figure 1(a).

The CME front was also detected by the Solar Orbiter/Metis instrument, in both the VL and UV channels, entering its FOV after 07:05 UT, following a western propagation direction (Figure 2); at that time, the longitudinal separation between Solar Orbiter and the Earth was approximately 26.73° east while the distance from the Sun was 0.62 au, resulting in an FOV spanning from about 3.7 $R_\odot$ to 6.9 $R_\odot$. During the event, Metis was performing observations dedicated to measuring the global coronal configuration and evolution before, during, and after CME events. The VL data were collected with a 30 minute cadence, a detector integration time (DIT) of 30 s, and an exposure time of 28 minutes; the number of DIT (NDIT), representing the number of images averaged on board, was set at 14. The VL detector, having a nominal plate scale of 10.14 arcsec pixel^{-1}, was configured with a 2×2 pixel binning, with resulting images of 1024×1024 pixels (Figure 2(a)). The UV data were acquired with a cadence $\tau_{UV} = 120$ s, DIT = 60 s, and NDIT = 1, corresponding to an exposure time of 60 s. The UV detector, with a nominal plate scale of 20.4 arcsec pixel^{-1}, was configured with a 4×4 pixel binning. Consequently, the resulting images were of 256×256 pixels (refer to Figure 2(b)). Due to the long duration of the chosen cadence and NDIT for this particular observation program, the VL channel could not be effectively utilized to deduce the physical parameters of the expanding CME/CME-driven shock (such as the electron density and the compression ratio). This limitation arises from the fact that every image results from an average of 14 data sets collected in a time interval of 28 minutes. During this period, as the CME structure extended away from the Sun, the images underwent a blurring effect, causing a displacement of approximately 50 pixels per cadence (assuming

an average speed of 570 km s^{-1}), thereby hindering accurate parameter inference. On the other hand, the UV images remained much less affected by this issue since the moving front, during the single acquisition with DIT = 60 s, shifted <2 pixels per cadence.

The detection of bands of fundamental (F) and harmonic (H) type II radio emissions by both ground- and space-based radio spectrographs, starting in the metric range at about 06:20 UT at a frequency of about 40 MHz (F), implied the propagation of a coronal shock into the interplanetary medium (e.g., Cane et al. 1981; Aurass et al. 1994). In this study, we have used ground-based radio spectrograph data obtained with the Compact Astronomical Low-frequency Low-cost Instrument for Spectroscopy in Transportable Observatory (CALLISTO; Benz et al. 2009) ASSA radio spectrometer[16] located in Australia with a time resolution of 0.25 s and a frequency range between 15 and 85 MHz (see Figure 3). The radio spectrum was integrated with data obtained at frequencies below 16 MHz by the Radio and Plasma Wave Investigation (SWAVES) instrument on board STEREO-A (Bougeret et al. 2008) with a temporal resolution of 60 s. In the SWAVES radio dynamic spectrum, the measurements in the 125 kHz–16.025 MHz range are from the High Frequency Receiver and those in the 2.5–160 kHz range from the Low Frequency Receiver.

A band-splitting in the dynamic spectrum of type II radio bursts is often observed, in which two similar branches of the same fundamental and/or harmonic lane drift toward lower frequencies with time. There are several interpretations of this phenomenon (see the discussion in Mancuso et al. 2019) but the most popular one, originally proposed by Smerd et al. (1975), suggests that the upper and lower frequencies of the

---

[16] http://www.e-callisto.org/.
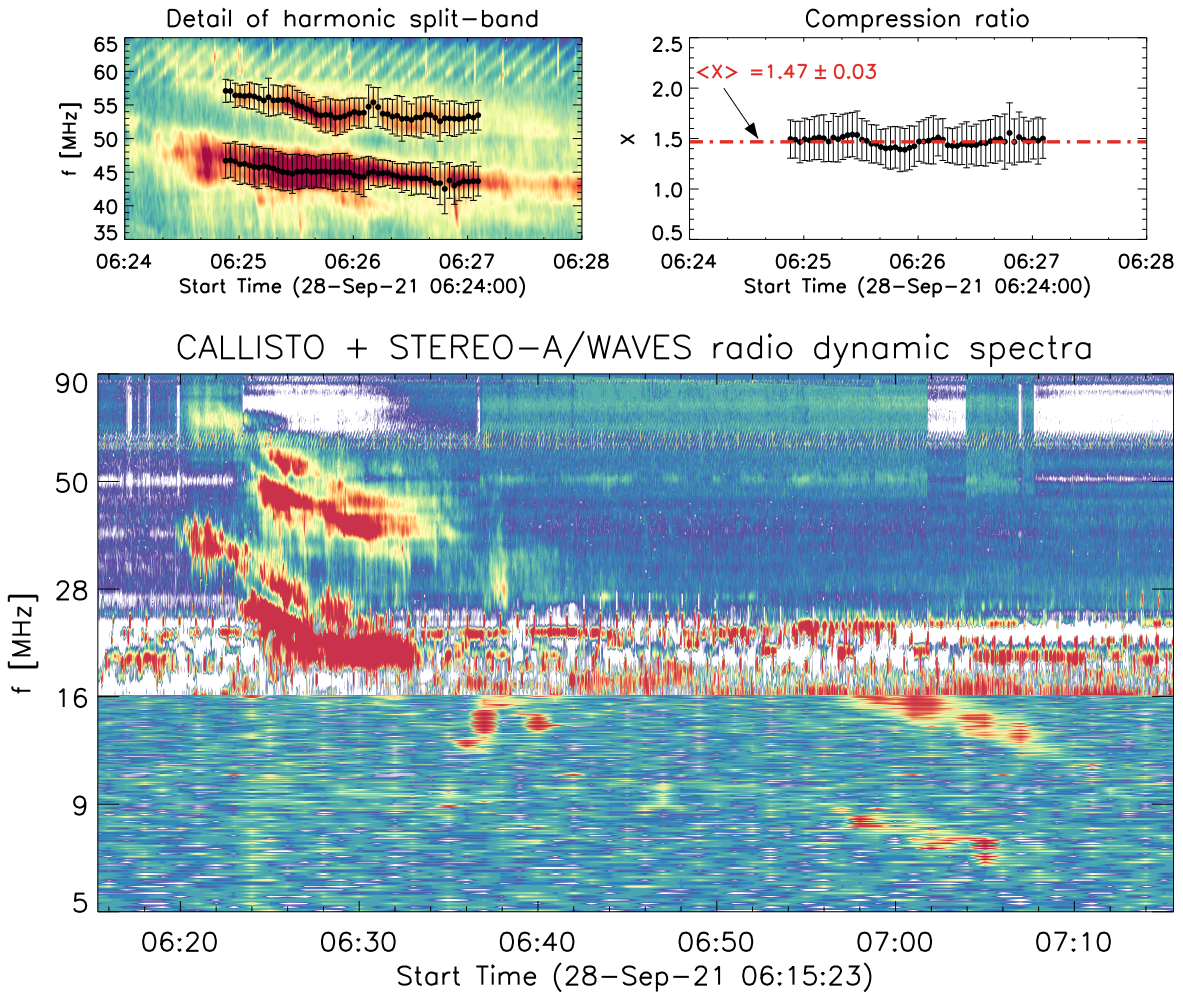
Figure 3. Composite dynamic radio spectrum of the type II radio burst observed on 2021 September 28 obtained by combining ground-based CALLISTO (>16 MHz) and space-based STEREO-A/WAVES (<16 MHz) data. At the top of the figure we show the splitting of the harmonic band together with an estimate of the compression ratio between about 06:25 UT and 06:27 UT.

band-splitting are simultaneously generated by the downstream and upstream components of a coronal shock, respectively, because of a density jump across the shock front. The compression ratio X_{radio} of the shock can be obtained from the band-splitting as

$$X_{\mathrm{radio}} = \frac{n_{\mathrm{e,D}}}{n_{\mathrm{e,U}}} = \left(\frac{f_{\mathrm{u}}}{f_{\mathrm{l}}}\right)^2, \qquad (1)$$

where $n_{\mathrm{e,D}}$ and $n_{\mathrm{e,U}}$ are the electron densities of the plasma in the downstream (D) and upstream (U) regions of the shock, respectively, and f_{u} is the upper branch frequency and f_{l} is the lower branch frequency of the type II radio burst.

From the metric radio spectrum of the upper and lower branches of the split harmonic band, we were able to evaluate with good accuracy the compression ratio in a 2 minute interval between about 6:25 UT and 6:27 UT, when the band-splitting was well defined in the radio dynamic spectrum (see top left and right panels of Figure 3). By using Equation (1), we were thus able to infer that the compression ratio was approximately constant, at least in this time interval, with an average value of $X_{\mathrm{radio}} = 1.47 \pm 0.03$. It is generally possible to obtain an approximate estimate of the source height of the type II radio burst, and thus the section of the shock responsible for its emission, by using a

plausible electron density model. In our case, by adopting a typical two-fold Newkirk (1961) model of a coronal streamer, $n_e = 8.4 \times 10^{[4+(4.32/R)]}$ cm^{-3}, with R in solar radii (e.g., Aurass & Mann 1987; Vršnak et al. 2002; Alissandrakis et al. 2023), we infer a corresponding height of about 2.3 $R_\odot$. On the other hand, since no evident band-splitting is observed in the decametric range, as shown in Figure 3 (although the upper split bands could have been too faint to be detected by the STEREO-A/WAVES instrument) and since the shock's strength is expected to somehow attenuate during its outward propagation in the upper corona (e.g., Bemporad & Mancuso 2011), X_{radio} will be considered, in the rest of the paper, as a plausible upper limit for the compression ratio along the front.

3. UV Data Analysis

The main purpose of this work is to demonstrate for the first time the possibility of estimating the evolution of the proton kinetic temperature of a CME-driven shock, considering it to be isotropic. This is achieved exclusively by using the coronagraphic data in the UV (H I Lyα) channel provided by the Solar Orbiter/Metis instrument and radio spectrograph data from CALLISTO and STEREO-A/WAVES. In this study, we limit our analysis to the time range between about 07:11 UT and 07:33 UT, corresponding to the time interval when it was

possible to follow the spatio-temporal evolution of the UV structures between about 4.5 $R_\odot$ and 6.9 $R_\odot$.

In the optically thin solar corona, H I Lyα line formation occurs (i) through collisional excitation, originating from the deexcitation of coronal atoms and/or ions that were excited earlier on by collisions with free electrons, and (ii) through radiative excitation, due to resonant scattering of photospheric and chromospheric radiation by neutral hydrogen atoms. The total observed intensity, I_{obs}, can thus be calculated by integrating the collisional (j_c) and radiative (j_r) emissivities, from each volume element of plasma, along the line of sight (LOS):

$$I_{obs} = I_{col} + I_{res} = \int_{LOS} (j_c + j_r)ds. \tag{2}$$

Since collisional processes in the solar corona contribute only 10% at low heliocentric heights and decrease by up to 1% at greater heights (Gabriel 1971), it is reasonable, in our case, to consider only the resonant scattering contribution for Lyα emission:

$$I_{obs} \approx I_{res} = \int_{LOS} j_r ds. \tag{3}$$

The radiative emissivity j_r is given by Noci et al. (1987):

$$j_r = h\lambda_0 n_H \frac{B_{12}}{4\pi} \int_\Omega p(\phi)d\omega \int_0^\infty I_\odot(\lambda - \delta\lambda)\Phi(\lambda - \lambda_0)d\lambda, \tag{4}$$

where h is the Planck constant, $\lambda_0 = 121.6$ nm is the reference wavelength of the transition, n_H is the neutral hydrogen number density, B_{12} is the Einstein coefficient for absorption for the H atom transition, $p(\phi)$ is a geometrical function for the scattering process, and ϕ is the angle between the LOS and the direction of the incident radiation. The last term under the integral sign is the so-called *Doppler dimming term*. This term contains the following quantities: (i) $I_\odot(\lambda - \delta\lambda)$, the intensity spectrum of the incident chromospheric radiation, (ii) $d\lambda = (\lambda_0/c)v_{rad}$, the Doppler shift of the incident profile due to the radial velocity v_{rad} of the scattering atoms, and (iii) $\Phi(\lambda - \lambda_0)$, the normalized coronal absorption profile in the direction of the incident radiation. The Doppler dimming term plays a pivotal role in deducing the ion temperature within the expanding plasma structure. A more compact way to express Equation (3), assuming that the excitation profile has a Gaussian shape, was given by Bemporad et al. (2021; see the paper for more details about the assumptions in deriving the following expressions):

$$I_{obs} = 0.83 \frac{h\lambda_0 B_{12}}{16\pi\sqrt{\pi}} R_H[T_e(\rho)]n_e(\rho)l(\rho)\frac{I_0}{\sqrt{\sigma_{disk}^2 + \sigma_{cor}^2}} D_D. \tag{5}$$

In the above equation, $n_p/n_e = 0.83$ is the usual approximation of fully ionized plasma with helium abundance equal to 10% in standard coronal conditions, $R_H[T_e(\rho)]$ is the neutral hydrogen ionization fraction depending on the electron temperature T_e, n_e is the electron density, and $l(\rho) = 2\{1 - [1 - (R_\odot/\rho)^2]^{1/2}\}(\rho/R_\odot)^2$ with ρ as the scattering distance on the plane of the sky. I_0 is the total intensity, $\sigma_{disk} = 0.34$ Å is the $1/e$ half-width of the Lyα chromospheric profile by neglecting possible nonthermal line broadenings

due to turbulence, waves, or other phenomena, $\sigma_{cor} = (\lambda_0/c)\sqrt{2k_B T_p/m_H}$, $\lambda_0 = 121.6$ nm, c is the light speed, k_B is the Boltzmann constant, m_H is the hydrogen mass, T_p is the proton temperature, and D_D is the Doppler dimming coefficient given, for any coronal spectral line radiatively excited by the disk emission in the same line, by

$$D_D = \exp\left[-\frac{v^2}{(\sigma_{disk}^2 + \sigma_{cor}^2)c^2/\lambda_0^2}\right], \tag{6}$$

where v is the outflow speed. The values of the Doppler dimming coefficient are always in the range $0 < D_D < 1$ ($D_D(v \to 0) = 1$ and $D_D(v \to \infty) \to 0$).

The presence of a moving shock front after 06:20 UT was confirmed by the simultaneous detection of a type II radio burst. Since the coronal magnetic field is mostly radial at the large heliocentric distances considered, we limit our discussion to the shock nose region, where we can assume quasi-parallel shock propagation with high confidence. Under this working hypothesis, in order to relate the plasma parameters in the upstream (subscript u) and downstream (subscript d) regions, we use the shock rest frame: in this frame, the plasma velocity v_u is larger than v_d. The Rankine–Hugoniot (RH) jump conditions for a parallel shock are

$$n_u v_u = n_d v_d \tag{7}$$

$$n_u v_u^2 + P_u = n_d v_d^2 + P_d \tag{8}$$

$$v_u\left(P_u\frac{\gamma}{\gamma - 1} + \frac{1}{2}n_u v_u^2\right) = v_d\left(P_d\frac{\gamma}{\gamma - 1} + \frac{1}{2}n_d v_d^2\right), \tag{9}$$

where n is the electron density, P is the plasma pressure, and γ is the adiabatic index. As Manchester et al. (2012) pointed out, the downstream plasma temperatures derived by using the RH equations may better represent postshock proton temperatures, while temperatures resulting from adiabatic compression could be more indicative of postshock electron temperatures.

By introducing an equation of state for a monatomic gas ($\gamma = 5/3$),

$$Pn^{-\gamma} = \text{constant}, \tag{10}$$

and by defining the density compression ratio as

$$X = \frac{n_d}{n_u} > 1, \tag{11}$$

the system of equations can be solved and written as

$$\frac{P_d}{P_u} = \frac{(\gamma + 1)X - (\gamma - 1)}{(\gamma + 1) - (\gamma - 1)X} \xrightarrow{\gamma=5/3} \frac{P_d}{P_u} = \frac{4X - 1}{4 - X}. \tag{12}$$

By assuming $P_d > P_u$, the upper limit for the compression ratio is

$$X < (\gamma + 1)/(\gamma - 1) = 4. \tag{13}$$

When the moving shock frame is considered and Equation (11) is used in Equation (7), we obtain

$$v_{w,d} = \frac{1}{X}[v_s(X - 1) + v_{w,u}], \quad \text{with } v_s > v_{w,d} > v_{w,u}, \tag{14}$$

where v_s is the shock speed and $v_{w,u}$ and $v_{w,d}$ are the upstream and downstream solar wind speeds, respectively. Using the expression for the Doppler dimming coefficient D_D given in
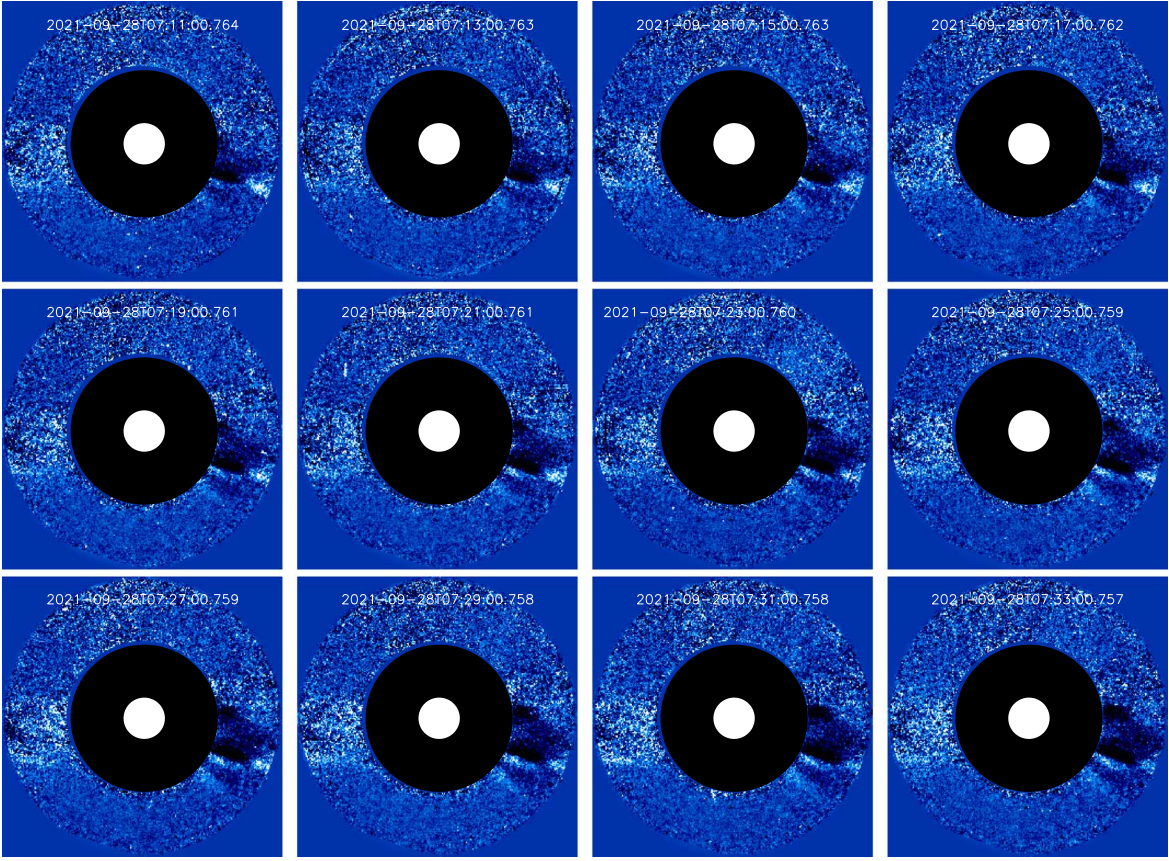
Figure 4. UV (Lyα) base difference images acquired by Metis in the time range where the expanding front was visible. The preevent image was taken at 05:29 UT. The white and black disks represent the Sun and the internal occulter, respectively.

Equation (6), we can calculate the ratio of the Doppler dimming factors downstream and upstream as

$$\frac{D_{\mathrm{D}}(v_{w,d})}{D_{\mathrm{D}}(v_{w,u})}$$
$$= \exp\left[-\frac{v_{w,d}^2}{(\sigma_{\mathrm{disk}}^2 + \sigma_{\mathrm{cor,d}}^2)c^2/\lambda_0^2} + \frac{v_{w,u}^2}{(\sigma_{\mathrm{disk}}^2 + \sigma_{\mathrm{cor,u}}^2)c^2/\lambda_0^2}\right],$$

(15)

where all the quantities defined so far are now referred to upstream and downstream regions.

From Equation (5) and Equation (11) we can express the UV image ratio, shown in Figure 4, as

$$\frac{I_{\mathrm{obs}}(t)}{I_{\mathrm{obs}}(t_0)} = \frac{\mathrm{UV}(t)}{\mathrm{UV}(t_0)} = \frac{R_{\mathrm{H},d}n_{e,d}\sqrt{\sigma_{\mathrm{disk}}^2 + \sigma_{\mathrm{cor,u}}^2}D_{\mathrm{D},d}}{R_{\mathrm{H},u}n_{e,u}\sqrt{\sigma_{\mathrm{disk}}^2 + \sigma_{\mathrm{cor,d}}^2}D_{\mathrm{D},u}}, \quad (16)$$

where the expanding structure in $\mathrm{UV}(t)$ ($t \in [07:11, 07:33]$ UT) is the downstream plasma and $\mathrm{UV}(t_0)$ ($t_0 = 05:29$ UT) is the upstream (unperturbed) plasma, renamed, for simplicity, as UV_d and UV_u, respectively. It should be noted that Equation (16) is independent of the total intensity I_0 present in Equation (5). Only values within the moving CME/CME-driven shock are considered, while the external ones are not taken into account.

We will further introduce the following hypotheses:

1. The preshock corona is approximately in thermodynamic equilibrium so that the electron temperature, $T_{e,u}$, is assumed to be similar to the proton temperature
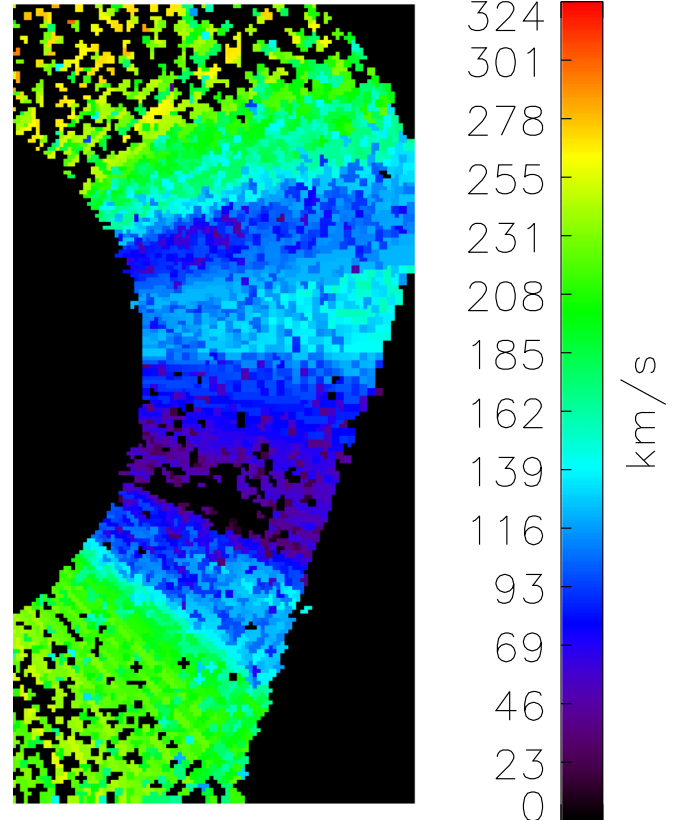
Figure 5. Detail of the 2D map of the solar wind speed, obtained by combining VL and UV data from Metis before the event, in the region crossed by the shock.

6
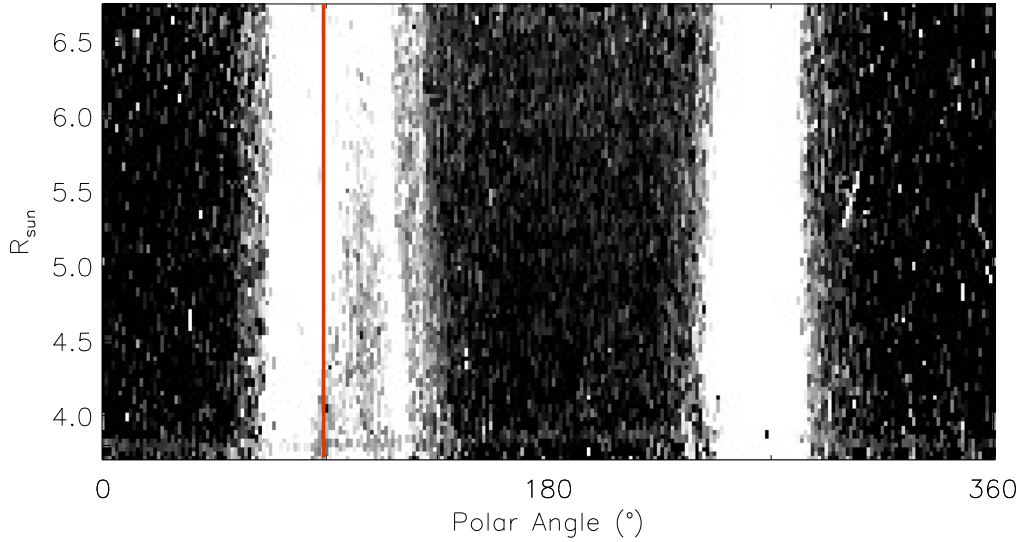
Figure 6. Example of a UV base difference image converted from Cartesian to polar coordinates; the red solid line identifies the slice used to build the J-map. The polar angle is measured clockwise starting from the north pole.

$(T_{p,u} = T_u)$, as found by Cranmer (2020) from the analysis of UVCS data.

2. The reduction of coronal emission, as shown in Figure 4, is mostly due to Doppler dimming.

3. We used $T_u = 10^6$ K (Strachan et al. 2002) and built the $v_{w,u}$ 2D map (e.g., Antonucci et al. 2005; Spadaro et al. 2007; Bemporad 2017; Dolei et al. 2018) as shown in Figure 5. To build this map we used chromospheric intensity[17] $I_0 = 7.0528 \times 10^{-3}$ W m^{-2}. We adopted the mean value of solar wind speed upstream calculated in the sheath region of the shock around its nose. The range of values is [80, 50] km s^{-1}, one different value for each frame considered in the analysis.

4. The downstream neutral hydrogen ionization fraction, $R_{H,d}$, is assumed to be equal to the upstream one ($R_{H,u} = R_{H,d}$), considering that the coronal plasma is collisionless, and that at around 4.5 $R_\odot$ the ionization time (estimated by using the CHIANTI Atomic Database; Del Zanna et al. 2021) is $\tau_i = 290$ s $> \tau_{UV} = 120$ s, and that τ_i increases at greater heliodistances (Withbroe et al. 1982).

5. We assume that downstream proton temperature $T_{p,d} = T_d > T_u$, and that $v_{w,u} < v_s$.

6. The estimate for the compression ratio X in the inner corona as derived from the analysis of the type II band-splitting in the radio band, $X = 1.47$ (see Figure 3), is employed as an upper limit for the compression ratio at the considered heliocentric distance.

Under these assumptions, Equation (16) is reduced to

$$\frac{UV_d}{UV_u} = X \frac{\sqrt{\sigma_{disk}^2 + \sigma_{cor,u}^2}}{\sqrt{\sigma_{disk}^2 + \sigma_{cor,d}^2}}$$

$$\times \exp\left[-\frac{v_{w,d}^2}{(\sigma_{disk}^2 + \sigma_{cor,d}^2)c^2/\lambda_0^2} + \frac{v_{w,u}^2}{(\sigma_{disk}^2 + \sigma_{cor,u}^2)c^2/\lambda_0^2} \right].$$

$$(17)$$

From Equation (17), the only unknown terms are $v_{w,d}$ and T_d (contained in $\sigma_{cor,d}$). We estimated the variation in speed by making the assumption that it was consistent across the front, resembling a quasi-spherical expansion. To derive this estimation, we utilized time–h maps (J-maps) dependent on the distance (h) from the center of the Sun. These maps were constructed by transforming base difference images (depicted in Figure 4) from Cartesian to polar coordinates. For each polar image, we selected a consistent slice containing a well-identified part of the front structure (as illustrated in Figure 6). Subsequently, we organized these slices into a time sequence, resulting in the J-map depicted in Figure 7(a).

The highest part of the visible expanding structure was chosen to measure the shock speed v_s. We followed the evolution (red asterisks in Figure 7(a)) and then fitted a second-order polynomial (red solid line in Figure 7(a)) to infer the parameters providing the shock speed v_s during its expansion. The uncertainties on the extrapolated speeds were derived by propagating the measured errors. To take into account the effect of identification of the expanding front in UV images, we assumed an uncertainty of 15%. The evolution of the shock speed, with error bars, is plotted in Figure 7(b). In this way, we can calculate the evolution of $v_{w,d}$ from Equation (14).

The evolution of the proton kinetic temperature, in the time range selected for the analysis, is then given by solving Equation (17).

Figure 8 shows the spatial evolution of T_p over time. We plot only the area where the expanding front was visible. The region where the hypotheses 1–6 are valid is bordered by the blue and light blue lines as the region behind the shock front has projected thickness equal to the distance crossed by the shock in a time equal to the ionization time τ_i. We assume here that this region represents the shock sheath region around the nose of the front.

Given the above hypotheses 1–6, these temperatures represent an upper limit. If we consider simple adiabatic compression heating, the temperature expected (an upper limit value) is $T_\gamma = T_{up}X^{\gamma-1} \sim 1.3$ MK. Upon comparing this value with the average temperatures, $\overline{T_d}$, within the shock sheath corresponding to the nose front region (Figure 9), it becomes

---

(a)

(b)
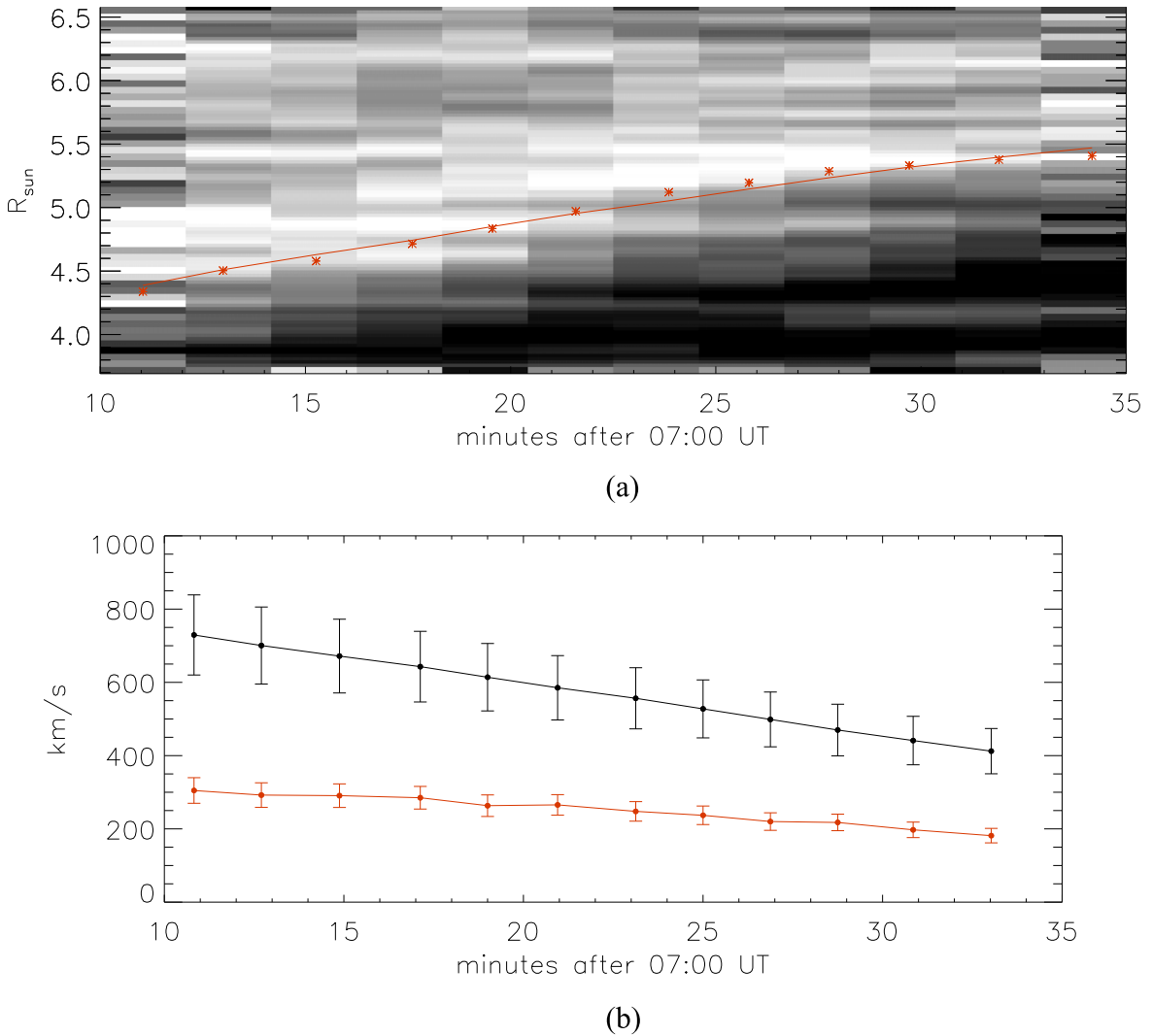
Figure 7. The J-map (a) from which we derived the evolution of the shock speed v_s (b). (a) The J-map captures the expansions of the front studied in the UV channel. To reconstruct the kinematic evolution of the expanding front, we employed a second-order polynomial fit (red solid line). (b) The evolution of the shock speed v_s (black solid line) calculated as the derivative of the function utilized to fit the kinematic evolution of the expanding front. The evolution of the downstream solar wind speed $v_{w,d}$ is depicted by the red solid line. Error bars corresponding to each speed measurement are also incorporated into the plot.

apparent that the latter temperatures are greater, and this suggests that shock heating is still occurring at these distances.

4. Summary and Conclusions

In this work, we have demonstrated for the first time the possibility of estimating the evolution of the 2D proton kinetic temperature in the CME-driven shock sheath by using only coronagraphic UV (Lyα) images and radio data from space- and ground-based observatories. This was done by using data taken by the Metis instrument and the CALLISTO-ASSA and STEREO-A/WAVES radio spectrometers. Generally, VL coronagraphic data and UV spectroscopic observations are used to infer coronal plasma parameters during the transit of a CME/CME-driven shock. In particular, the plasma temperatures during the expansion phase of a CME typically rely on the analysis of spectroscopic data. These data are predominantly obtained through the UVCS spectrometer. Alternatively, electron temperatures have been deduced by collecting data on the intensities of various spectral lines produced by different ions detected by the spectrometer: the temperature is determined by finding the

best match between the observed ionization states and the excitation rates required to account for the observed emissions.

The Metis instrument represents the pioneering solar coronagraph created for a space mission and is capable of concurrently acquiring images of the off-limb solar corona using visible and ultraviolet wavelengths. However, the instrument does not have a spectrometer, so plasma temperatures cannot be measured directly. This is because the intensity of Lyα depends not only on the plasma's electron temperature and density but also on various other factors, including proton kinetic temperature. In particular, Manchester et al. (2012) showed that during the passage of a shock, proton temperatures increase more than electron temperatures because protons primarily absorb the kinetic energy at the shock while electrons are basically heated by adiabatic compression.

The event studied in this work was observed on 2021 September 28 by different space-based coronagraphs and it involved a CME and a CME-driven shock. The presence of the coronal/interplanetary shock was confirmed by the detection of a metric/decametric type II radio burst. A compression ratio $X = 1.47 \pm 0.03$ at about 2.3 $R_\odot$ is estimated from the observed
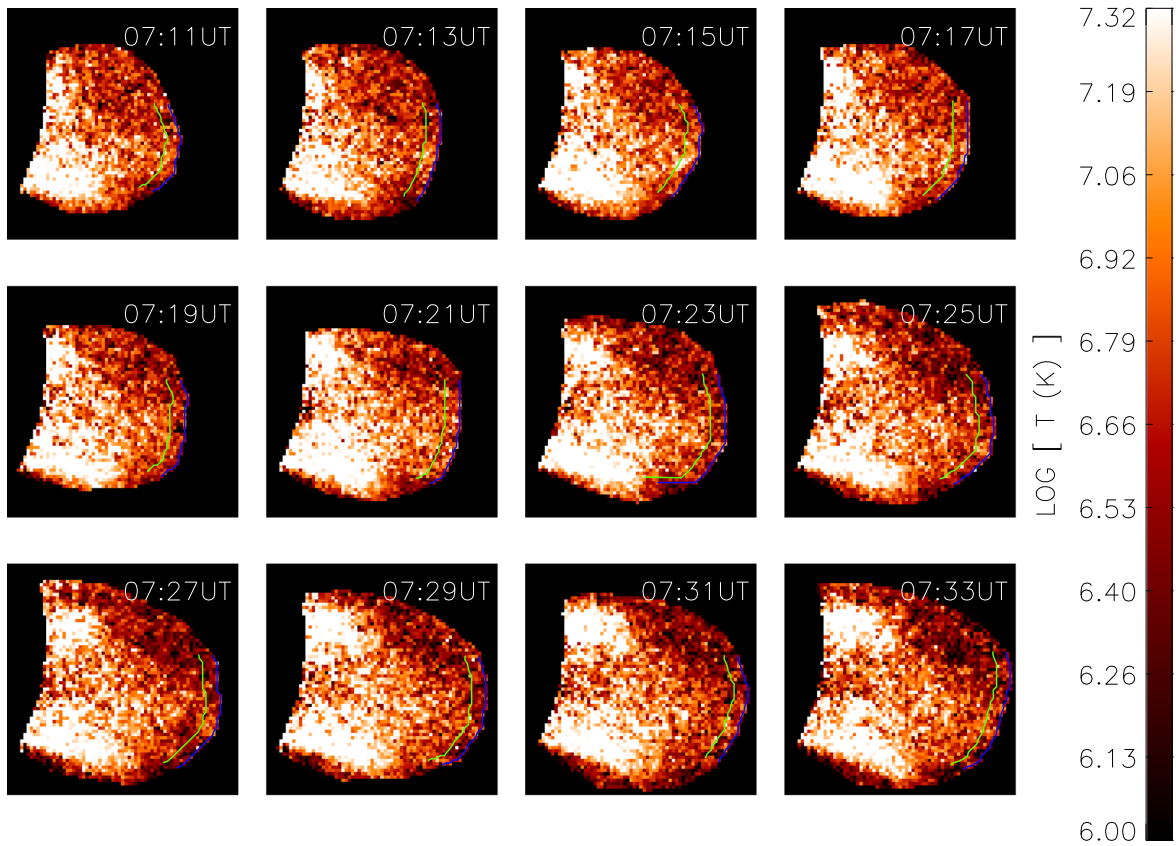
Figure 8. The evolution of the proton kinetic temperature during the expansion of the front. The blue and green solid lines border the sheath region where the hypotheses 1–6 are valid.
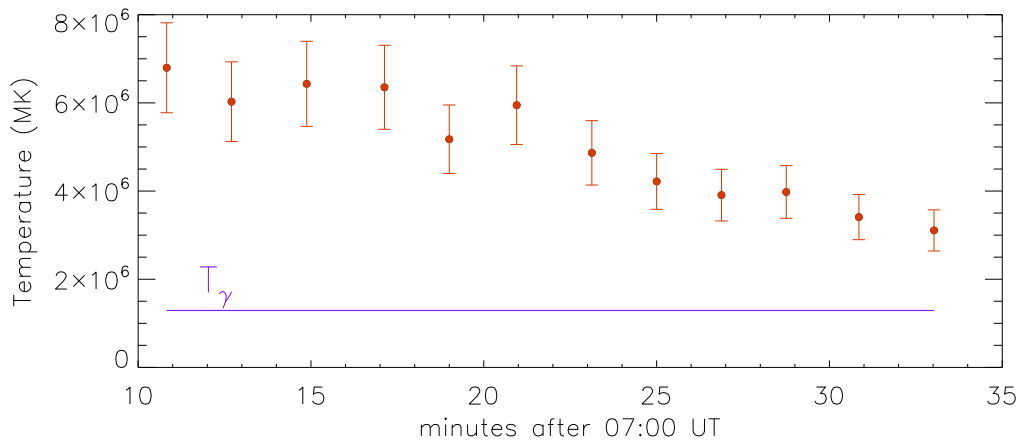
Figure 9. The average proton kinetic temperature, within the shock sheath corresponding to the nose front region, as a function of time. The violet line represents the adiabatic temperature T_γ.

band-splitting of the harmonic band and by adopting a typical two-fold Newkirk (1961) model of a coronal streamer. This value was assessed to be almost constant in the 2 minute interval when the band-splitting was well-defined.

We analyzed the event in the time range during which the entire expanding structure was visible in the FOV of Metis, between about 4.5 $R_\odot$ and 6.9 $R_\odot$. In order to infer the evolution of the proton kinetic temperature within the CME-driven shock sheath, around the nose region of the expanding front, we assumed the estimate for the electron-density compression ratio X, which was thus effectively used as an upper limit for the compression ratio at greater heliocentric

distances. Higher up in the corona, the shock nose was assumed to expand with a quasi-parallel geometry. Under this plausible hypothesis, from the RH jump conditions, the assumption of an adiabatic index for monatomic gas, and forcing the upstream gas pressure to be larger than the downstream pressure, we were able to express the downstream solar wind speed, $v_{w,d}$, as a function of the compression ratio X, the upstream solar wind speed $v_{w,u}$, and the shock speed v_s. The last physical parameter was inferred by using J-maps and by fitting the selected positions of the structure with a second-order polynomial. In the time interval analyzed (22 minutes) we found a speed decreasing from $\sim\!740 \pm 110$ km s^{-1} to $\sim\!400 \pm 60$ km s^{-1}.

Table 1
Comparison between Parameters, Related to Downstream Temperature, Obtained in Different Studies

Parameter	Bemporad & Mancuso (2010)	Ma et al. (2011)	Bemporad et al. (2014)	Frassati et al. (2020)	This Study
Geometry	$\angle$	$\angle$	$\parallel$	$\perp$	$\parallel$
d ($R_\odot$)	4.1	1.2	2.6	1.2	4.5–6.9
X	2.06	1.56	3.78	1.23	1.47
T_u (MK)	0.23	1.8	1.49	1.78	1.0
T_d (MK)	1.88	2.8	25.3	2.75	6.8–3.1
v_s (km s^{-1})	800	600	1575	950	740–400
T_d/T_u	8.2	1.56	17	1.55	6.8–3.1
T_γ (MK)	0.37	2.42	3.61	2.04	1.3

This decrease can be due to the different conditions of the coronal plasma and coronal structures crossed by the shock that decelerates the expanding front.

From the approximate expression for the Doppler dimming coefficient (Equation (6)) and a set of plausible hypotheses (1–6 in Section 3), we were able to express the UV image ratio as a function of the downstream and upstream Doppler dimming coefficients, ($D_{D,d}$ and $D_{D,u}$, respectively), and the compression ratio X inferred from the radio data. Finally, the proton kinetic temperature over time is obtained by solving Equation (17). By calculating the average values of this temperature, $\overline{T_d}$, around the nose of the front over time, and by comparing them with that expected from a simple adiabatic compression, we further found that significant shock heating was still going on at these distances and that protons are most affected by the heating caused by the passage of the shock. In fact, the electron thermal speed is significantly higher than the shock speed measured here ($v_{e,\text{th}} \sim 5500$ km s$^{-1} \gg v_s$), whereas the proton thermal speed is lower ($v_{p,\text{th}} \sim 129$ km s$^{-1} < v_s$).

Studies of CME-driven shock sheath temperatures through remote-sensing observations are rare compared to in situ ones. The high-resolution capabilities provided by instruments such as the AIA telescope and the differential emission measure technique are seldom applicable for studying shocks because, statistically, these phenomena tend to occur at distances greater than about 1.5 $R_\odot$, falling outside the field of view of the EUV instruments, as demonstrated by Gopalswamy et al. (2013). Similarly, previous studies with data from UVCS and LASCO were necessarily limited by the fact that the UVCS slit covered only a limited FOV. So the comparison of the results presented in this work with the previous studies may be biased and also affected by the possibly different shock geometry. Table 1 shows a collection of the different parameters derived from previous studies and this one. The only valid direct comparison can properly be made with the findings of Bemporad et al. (2014), mainly due to the similarities in their shock geometry and our event. Their study revealed a downstream temperature (T_d) approximately 17 times higher than the upstream temperature (T_u). These higher values are likely attributed to the greater shock speed and compression ratio of their specific event. The other studies, on the other hand, despite variations in the assumed shock geometry, exhibit a remarkable similarity in the parameters X and v_s when compared to the present study. Nevertheless, it should be noted that variations in findings across studies can also be influenced by various factors affecting the outcomes. These factors include the state of the surrounding environment varying

with the solar activity cycle, leading to variations in coronal density, preexisting structures (such as streamers, pseudo-streamers, and coronal holes), magnetic field configuration, solar wind speed, as well as differing assumptions made during the analysis.

This analysis could potentially be extended to future data sets obtained from UV coronagraphs, thus enabling the estimation of the 2D proton kinetic temperature across the entire shock front.

ORCID iDs

Federica Frassati https://orcid.org/0000-0001-9014-614X
Alessandro Bemporad https://orcid.org/0000-0001-5796-5653
Salvatore Mancuso https://orcid.org/0000-0002-9874-2234
Silvio Giordano https://orcid.org/0000-0002-3468-8566
Vincenzo Andretta https://orcid.org/0000-0003-1962-9741
Aleksandr Burtovoi https://orcid.org/0000-0002-8734-808X
Vania Da Deppo https://orcid.org/0000-0001-6273-8738
Silvano Fineschi https://orcid.org/0000-0002-2789-816X
Catia Grimani https://orcid.org/0000-0002-5467-6386
Salvo Guglielmino https://orcid.org/0000-0002-1837-2262
Petr Heinzel https://orcid.org/0000-0002-5778-2600
Giovanna Jerse https://orcid.org/0000-0002-0764-7929
Federico Landini https://orcid.org/0000-0001-8244-9749
Alessandro Liberatore https://orcid.org/0000-0002-0016-7594
Giampiero Naletto https://orcid.org/0000-0003-2007-3138
Gianalfredo Nicolini https://orcid.org/0000-0002-9459-3841
Maurizio Pancrazzi https://orcid.org/0000-0002-3789-2482
Paolo Romano https://orcid.org/0000-0001-7066-6674

Marco Romoli ⦿ https://orcid.org/0000-0001-9921-1198
Giuliana Russano ⦿ https://orcid.org/0000-0002-2433-8706
Clementina Sasso ⦿ https://orcid.org/0000-0002-5163-5837
Daniele Spadaro ⦿ https://orcid.org/0000-0003-3517-8688
Marco Stangalini ⦿ https://orcid.org/0000-0002-5365-7546
Roberto Susino ⦿ https://orcid.org/0000-0002-1017-7163
Luca Teriaca ⦿ https://orcid.org/0000-0001-7298-2320
Michela Uslenghi ⦿ https://orcid.org/0000-0002-7585-8605
Luca Zangrilli ⦿ https://orcid.org/0000-0002-4184-2031

References

Akmal, A., Raymond, J. C., Vourlidas, A., et al. 2001, ApJ, 553, 922
Alissandrakis, C., Hillaris, A., Bouratzis, C., & Armatas, S. 2023, Univ, 9, 442
Antonucci, E., Abbo, L., & Dodero, M. A. 2005, A&A, 435, 699
Antonucci, E., Romoli, M., Andretta, V., et al. 2020, A&A, 642, A10
Aurass, H., Klein, K. L., & Mann, G. 1994, in ESA Special Publication 373, Solar Dynamic Phenomena and Solar Wind Consequences, the Third SOHO Workshop, ed. J. J. Hunt (Paris: ESA), 95
Aurass, H., & Mann, G. 1987, SoPh, 112, 359
Bemporad, A. 2008, ApJ, 689, 572
Bemporad, A. 2017, ApJ, 846, 86
Bemporad, A. 2022, Symmetry, 14, 468
Bemporad, A., Giordano, S., Zangrilli, L., & Frassati, F. 2021, A&A, 654, A58
Bemporad, A., & Mancuso, S. 2010, ApJ, 720, 130
Bemporad, A., & Mancuso, S. 2011, ApJL, 739, L64
Bemporad, A., Pagano, P., & Giordano, S. 2018, A&A, 619, A25
Bemporad, A., Raymond, J., Poletto, G., & Romoli, M. 2007, ApJ, 655, 576
Bemporad, A., Susino, R., & Lapenta, G. 2014, ApJ, 784, 102
Benz, A. O., Monstein, C., Meyer, H., et al. 2009, EM&P, 104, 277
Bougeret, J. L., Goetz, K., Kaiser, M. L., et al. 2008, SSRv, 136, 487
Brueckner, G. E., Howard, R. A., Koomen, M. J., et al. 1995, SoPh, 162, 357
Cai, Q.-w., Wu, N., & Lin, J. 2016, ChA&A, 40, 352
Cane, H. V., Stone, R. G., Fainberg, J., et al. 1981, GeoRL, 8, 1285
Ciaravella, A., Raymond, J. C., van Ballegooijen, A., et al. 2003, ApJ, 597, 1118
Cranmer, S. R. 2020, ApJ, 900, 105
Del Zanna, G., Dere, K. P., Young, P. R., & Landi, E. 2021, ApJ, 909, 38
Dolei, S., Susino, R., Sasso, C., et al. 2018, A&A, 612, A84
Domingo, V., Fleck, B., & Poland, A. I. 1995, in The High Latitude Heliosphere, ed. R. G. Marsden (Dordrecht: Springer)
Fineschi, S., Naletto, G., Romoli, M., et al. 2020, ExA, 49, 239
Frassati, F., Mancuso, S., & Bemporad, A. 2020, SoPh, 295, 124
Gabriel, A. H. 1971, SoPh, 21, 392
Giordano, S., Ciaravella, A., Raymond, J. C., Ko, Y. K., & Suleiman, R. 2013, JGRA, 118, 967
Gopalswamy, N., Xie, H., Mäkelä, P., et al. 2013, AdSpR, 51, 1981
Hansen, R. T., Garcia, C. J., Grognard, R. J. M., & Sheridan, K. V. 1971, PASA, 2, 57
Hyder, C. L., & Lites, B. W. 1970, SoPh, 14, 147
Kohl, J. L., Esser, R., Gardner, L. D., et al. 1995, SoPh, 162, 313
Lemen, J. R., Title, A. M., Akin, D. J., et al. 2012, SoPh, 275, 17
Ma, S., Raymond, J. C., Golub, L., et al. 2011, ApJ, 738, 160
Machol, J., Snow, M., Woodraska, D., et al. 2019, E&SS, 6, 2263
Manchester, W. B. I., van der Holst, B., Tóth, G., Tóth, G., & Gombosi, T. I. 2012, ApJ, 756, 81
Mancuso, S. 2011, SoPh, 273, 511
Mancuso, S., & Avetta, D. 2008, ApJ, 677, 683
Mancuso, S., Frassati, F., Bemporad, A., & Barghini, D. 2019, A&A, 624, L2
Mancuso, S., Raymond, J. C., Kohl, J., et al. 2002, A&A, 383, 267
Morgan, H., Habbal, S. R., & Woo, R. 2006, SoPh, 236, 263
Müller, D., Cyr, O. C., St., Zouganelis, I., et al. 2020, A&A, 642, A1
Müller, D., Nicula, B., Felix, S., et al. 2017, A&A, 606, A10
Newkirk, G., Jr. 1961, ApJ, 133, 983
Noci, G., Kohl, J. L., & Withbroe, G. L. 1987, ApJ, 315, 706
Raymond, J. C., Ciaravella, A., Dobrzycka, D., et al. 2003, ApJ, 597, 1106
Smerd, S. F., Sheridan, K. V., & Stewart, R. T. 1975, ApL, 16, 23
Spadaro, D., Susino, R., Ventura, R., Vourlidas, A., & Landi, E. 2007, A&A, 475, 707
Strachan, L., Suleiman, R., Panasyuk, A. V., Biesecker, D. A., & Kohl, J. L. 2002, ApJ, 571, 1008
Susino, R., & Bemporad, A. 2016, ApJ, 830, 58
Susino, R., Bemporad, A., & Dolei, S. 2014, ApJ, 790, 25
Vršnak, B., Magdalenić, J., Aurass, H., & Mann, G. 2002, A&A, 396, 673
Withbroe, G. L., Kohl, J. L., Weiser, H., & Munro, R. H. 1982, SSRv, 33, 17
Ying, B., Bemporad, A., Feng, L., et al. 2020, ApJ, 899, 12